Design and operation of antiresonant Fabry–Perot saturable semiconductor absorbers for mode-locked solid-state lasers

L. R. Brovelli and U. Keller

Swiss Federal Institute of Technology, Institute of Quantum Electronics, ETH Hönggerberg, CH-8093 Zurich, Switzerland

T. H. Chiu

AT&T Bell Laboratories, Holmdel, New Jersey 07733

Received March 11, 1993; revised manuscript received August 22, 1994

The antiresonant Fabry–Perot saturable semiconductor absorber (A-FPSA) has been successfully used to passively mode lock many different solid-state lasers. The main advantage of the A-FPSA is that important operation parameters such as the saturation intensity, losses, and impulse response can be influenced by the material and the device parameters and can be adapted to the requirements of solid-state lasers. We present a detailed quantitative discussion of the operation parameters, derive simple design rules, and show that the contribution of the A-FPSA to the starting and the stabilization of mode locking is much larger than the effect of Kerr lensing in a mode-locked Nd:YAG laser.

1. INTRODUCTION

Over the past several years a dramatic revolution in the generation of ultrashort optical pulses with passively mode-locked solid-state lasers has been initiated by the invention of several new mode-locking schemes, such as additive-pulse mode locking,[1–3] Kerr-lens mode locking[4–7] (KLM), and resonant passive mode locking.[8] Previously, passive mode locking of solid-state lasers was considered difficult, if not impossible, because of the lack of a suitable fast saturable absorber. KLM is the simplest mode-locking technique but is generally not self-starting and is rather weak in the picosecond regime. For starting and stabilizing the pulsation, a fast saturable absorber with low losses and an appropriate saturation intensity is required. Within an all-solid-state ultrafast laser technology semiconductor saturable absorbers seem promising, since they have the advantages that they are compact and fast and can cover a wavelength range from the visible to the infrared. For example, a femtosecond diode-pumped Cr:LiSAF laser with a multiple-quantum-well (MQW) saturable absorber was recently demonstrated.[9]

Normally, however, semiconductor materials are not well matched to the characteristics required for solid-state lasers; i.e., the semiconductors tend to have too much optical loss, too low a saturation intensity, and too low a damage threshold for typical solid-state lasers such as Nd:YAG. These issues are resolved by use of the recently developed antiresonant Fabry–Perot saturable semiconductor absorber[10,11] (A-FPSA), which integrates the semiconductor absorber inside a Fabry–Perot cavity that is operated at antiresonance (Fig. 1). Antiresonance entails that the intensity inside the Fabry–Perot be smaller than the incident intensity, which decreases the device loss and increases the saturation intensity. The damage threshold is determined by the top reflector, which is typically an evaporated dielectric mirror similar to other mirrors inside the laser cavity.

In practical use the A-FPSA is a nonlinear mirror, typically $\approx$400 μm thick, which simply replaces one of the laser cavity mirrors to passively mode lock a cw pumped laser. The nonlinear reflectivity change in the A-FPSA is due to band filling, in which the absorption is bleached with the photoexcited carriers because of the Pauli exclusion principle. The A-FPSA, used as a simple end mirror in a laser cavity, has successfully passively mode locked many different neodymium-doped solid-state lasers such as Nd:YLF, Nd:YAG,[11–13] Nd:fiber,[14] and Nd:glass[15,16] with picosecond to shorter-than-100-fs pulses. In an all-solid-state ultrafast laser technology the A-FPSA is a low-loss intracavity saturable absorber for which the mode locking is always self-starting and stable against Q switching. The main reason is that the operation parameters, such as saturation intensity, insertion losses, and impulse response of the A-FPSA, can be custom designed and adapted to the requirements of solid-state lasers. The impulse response shows a bitemporal behavior, i.e., a slow time constant, which is due to carrier recombination for efficient starting of the mode locking and the generation of picosecond pulses, as well as a fast time constant, which is due to carrier thermalization for further pulse shortening and sustaining of pulses shorter than 100-fs.

The samples that we have built have a bottom mirror that consists of 16 pairs of GaAs and AlAs quarter-wave layers that form a Bragg mirror with a center wavelength of 1050 nm and an approximately 100-nm bandwidth (see Fig. 1). On top of the mirror is grown an absorber, consisting of a strained InGaAs–GaAs superlattice; the indium content in the wells determines the absorption edge, which can be varied from 900 nm to potentially 2 μm.

0740-3224/95/020311-12$06.00

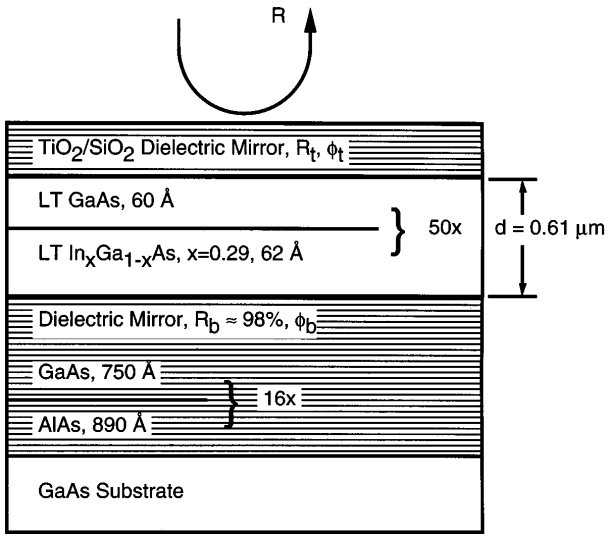

Fig. 1. Structure of an A-FPSA designed for an operation wavelength of $\approx 1\ \mu$m.

Finally, a top mirror consisting of three or four pairs of SiO_2 and TiO_2 quarter-wave layers is evaporated on top of the absorber.

In addition, the absorber is grown at low temperatures (i.e., between 200 and 400 °C instead of at >600 °C; see Refs. 17 and 18). The advantages of low-temperature (LT) molecular-beam-expitaxy growth are twofold. First, incorporation of excess arsenic in form of interstitials and clusters leads to interband states that drastically reduce the lifetime of photogenerated carriers and thus the absorber recovery time, an essential parameter for mode-locking performance.[11] It has been shown that this lifetime depends on the growth temperature in a highly controlled and reproducible manner. Second, the degradation in surface morphology of InGaAs–GaAs MQW's for normal growth conditions, which would result in high scattering losses, is reduced, since the defects have dimensions that are much smaller than the optical wavelength, and no cross-hatched roughness is present in our LT-grown MQW's.[17,18]

In this paper we present a detailed quantitative discussion of the operation parameters of an A-FPSA based on accurate measurements of the low-intensity reflectivity, the absorption recovery time, and the saturation fluence of samples in which the top reflector is replaced by an antireflection (AR) coating. Operation of an A-FPSA in a real mode-locked Nd:YAG laser is discussed and compared with the effect of nonlinear gain change that is due to Kerr lensing. It can be shown that the A-FPSA leads typically to a 1000-times-higher mode-locking driving force and to a larger total reduction in losses for pulsed operation than does the Kerr effect.

The paper is organized as follows: in Section 2 the most important parameters of a saturable absorber are introduced, and their significance for mode-locking performance is discussed. Since all the measurements have been performed on AR-coated samples, we show how to derive the saturation behavior of corresponding high-reflectivity- (HR-) coated A-FPSA's. The measurements and results are described in Section 3. Using the example of a mode-locked Nd:YAG laser (Section 4), we compare the nonlinear change in losses of the A-FPSA with the change in gain that is due to KLM and show that the former always has a stronger effect in the picosecond regime and leads to a much stronger mode-locking driving force. These results also explain why mode locking with an A-FPSA is always self-starting. Furthermore, the stability against self-Q-switching and the mode-locking buildup time are discussed quantitatively and compared with the experiments. The use of A-FPSA's in the femtosecond regime is discussed in Section 5, where recent experiments on Nd:glass lasers are reviewed. In Section 6 the results are summarized and discussed.

2. THEORY: OPERATION OF A-FPSA'S

A. Fabry–Perot Cavity at Antiresonance

The A-FPSA is an absorber sandwiched between two HR Bragg mirrors forming a Fabry–Perot cavity, which is operated at antiresonance (see Fig. 1). The total phase change of an electromagnetic wave with vacuum wave number k after one round trip inside the semiconductor absorber with thickness d and refractive index n is

$$\Phi_{rt} = 2nkd + \phi_b + \phi_t, \tag{1}$$

with the phase of the reflectivities of the top and the bottom mirror being ϕ_t and ϕ_b, respectively. The thickness of the absorber layer is designed so that the operating wavelength of the laser is antiresonant with the Fabry–Perot cavity, i.e., $d = d_a$, with

$$\Phi_{rt,a} = 2nkd_a + \phi_b + \phi_t = (2m - 1)\pi, \qquad m = 1, 2, 3, \ldots . \tag{2}$$

The field therefore is in antiphase after one round trip in the Fabry–Perot cavity and interferes destructively, which reduces the average intensity. Contrary to the sharp resonance, the antiresonance in a high-finesse Fabry–Perot cavity is a broad maximum of the reflectivity as a function of wavelength or a broad minimum of the transmission. Therefore Eq. (2) provides noncritical design tolerances for the thickness d_a. Within the stop band of the Bragg mirrors the phases ϕ_t and ϕ_b can be written as linear functions of the wave number:

$$\phi_t = 2(k - k_B)n_{\mathrm{eff}}{}^t L_{\mathrm{eff}}{}^t, \qquad \phi_b = \pi + 2(k - k_B)n_{\mathrm{eff}}{}^b L_{\mathrm{eff}}{}^b, \tag{3}$$

with the Bragg wave number k_B designed to be the same for both mirrors. Equations (3) define the effective penetration depth $n_{\mathrm{eff}}L_{\mathrm{eff}}$ of a Bragg mirror: the dependence of the phase on the wave number as given in Eqs. (3) is equivalent to the situation with a constant phase but with the interface shifted by a distance L_{eff} into the mirror with effective refractive index n_{eff}. At the Bragg wavelength the phase of the reflectivity is either 0 if the first layer is one with a lower refractive index (as is the case for the top mirror, where the first layer on the absorber is SiO_2 with $n = 1.45$ followed by TiO_2 with $n = 2.4$) or π if the first layer is one with a higher refractive index (as is the case for the bottom mirror, where the first layer under the absorber is GaAs with $n = 3.49$ followed by AlAs with $n = 2.94$). From Eqs. (2) and (3) we obtain the free

spectral range, i.e., the wavelength interval between two neighboring resonances:

$$\Delta\lambda = \lambda^2/2L_{\mathrm{opt}}\,, \tag{4}$$

with the optical length

$$L_{\mathrm{opt}} = nd + {n_{\mathrm{eff}}}^t {L_{\mathrm{eff}}}^t + {n_{\mathrm{eff}}}^b {L_{\mathrm{eff}}}^b\,. \tag{5}$$

From Eqs. (3) we see that the effective penetration depth into a Bragg mirror is given by half of the derivative of the phase with respect to the wave number. For a distributed Bragg reflector of infinite thickness adjacent to a medium with the same effective refractive index, as is the case in semiconductor distributed-feedback and distributed-Bragg-reflector lasers, the penetration depth can be calculated from coupled-mode theory[19]:

$$n_{\mathrm{eff}} L_{\mathrm{eff}} = \frac{n_{\mathrm{eff}}\lambda_B}{4\Delta n}\,, \tag{6}$$

with the Bragg wavelength λ_B, the difference in refractive index of the two layers $\Delta n = n_2 - n_1$, and the effective refractive index

$$n_{\mathrm{eff}} = \frac{d_1 n_1 + d_2 n_2}{d_1 + d_2} = \frac{\lambda_B}{2(d_1 + d_2)}\,, \tag{7}$$

where d_1 and d_2 are the thicknesses of the layers. Although it is widely used, Eq. (6) is not correct for an arbitrary Bragg mirror, since it neglects the interface between the mirror and the adjacent medium. In fact the error introduced by this simplification can be a factor of 2, as we showed in Ref. 20, where we derived the following more precise formulas for the reflectivity of a Bragg medium next to a medium with refractive index n by using a combination of coupled-mode theory and a matrix formalism:

$$n_{\mathrm{eff}} L_{\mathrm{eff}} = \frac{n\lambda_B}{4\Delta n} \tag{8}$$

if the first layer in the Bragg stack is one with a higher refractive index and

$$n_{\mathrm{eff}} L_{\mathrm{eff}} = \frac{\lambda_B \Delta n}{2\pi^2 n} + \frac{{n_{\mathrm{eff}}}^2 \lambda_B}{4n\Delta n} \tag{9}$$

if the first layer is one with a lower refractive index. The results from these equations were compared with numerical calculations. The difference was found to be only a few percent.[20] From Eqs. (5), (8), and (9) we can calculate the free spectral range of A-FPSA's operating at $\lambda = 1050$ nm (Fig. 1) and obtain $\Delta\lambda = 140$ nm for $n = 3.4$ of the LT-grown absorber, with penetration depths into the top mirror of 0.32 μm and into the bottom mirror of 1.53 μm.

In our case, however, the spectral range is also limited by the bandwidth of the HR stop band of the bottom mirror, which is given by[21]

$$\Delta\lambda = \frac{4\lambda_B}{\pi}\,\sin^{-1}\left(\frac{n_2 - n_1}{n_2 + n_1}\right). \tag{10}$$

At the edges of the stop band the reflectivity rapidly goes to zero, and the linear approximation of the phase, Eqs. (3), is no longer correct. We obtain for the bottom mirror with $n_2 = 3.49$ (GaAs) and $n_1 = 2.94$ (AlAs) a spectral bandwidth of $\Delta\lambda = 115$ nm, thus slightly smaller than the theoretical free spectral range of the Fabry–Perot cavity. In contrast, the bandwidth of the top mirror with $n_1 = 1.45$ (SiO_2) and $n_2 = 2.4$ (TiO_2) is calculated to be $\Delta\lambda = 330$ nm, thus setting no limit on the total bandwidth of the A-FPSA. The calculated available spectral range is in good agreement with our measurements (see Section 3) and numerical calculations (see Subsection 2.D).

B. Nonlinear Reflectivity Change

For use in a passively mode-locked laser system the most important parameters of a saturable absorber are the recovery time, the saturation intensity, and the insertion losses. With an A-FPSA it is possible to custom design these parameters and to adapt them to the requirements of solid-state lasers. In this section we derive simple formulas that permit the calculation of the effective saturation intensity, the mode-locking driving force, and the losses of an A-FPSA from the measured material parameters.

We consider an A-FPSA as depicted in Fig. 1. If the reflectivities of the top and the bottom mirrors are known, the reflectivity of the entire structure can be calculated from well-known Fabry–Perot formulas[22] as

$$R = \frac{[\sqrt{R_t} + \sqrt{R_b}\,\exp(-2\alpha d)]^2 - 4\sqrt{R_t R_b}\,\exp(-2\alpha d)\cos^2(\Phi_{rt}/2)}{[1 + \sqrt{R_t R_b}\,\exp(-2\alpha d)]^2 - 4\sqrt{R_t R_b}\,\exp(-2\alpha d)\cos^2(\Phi_{rt}/2)}\,, \tag{11}$$

with Φ_{rt} given by Eq. (1) or (2) for the special case of antiresonance within the stop bands of the Bragg mirrors and with the thickness d, the refractive index n, and the amplitude absorption coefficient α of the absorber. R_t and R_b denote the intensity reflectivities of the top and the bottom mirrors, respectively. To measure the saturation fluence directly on an A-FPSA would be difficult, because the saturation fluence is too high to be obtained from a laser outside the cavity and the reflectivity changes would be very low, i.e., less than 1%. We therefore performed the measurements on samples in which the top reflector was replaced with an AR coating, eliminating any Fabry–Perot effects. Consequently we have to calculate the ratio between the intensity distribution inside an A-FPSA $I_{\mathrm{HR}}(z)$ and inside an AR-coated sample $I_{\mathrm{AR}}(z)$ for the same incident intensity. This ratio is given by

$$I_{\mathrm{HR}}(z) = \xi I_{\mathrm{AR}}(z)\,, \tag{12}$$

where

$$\xi = \frac{1 - R_t}{[1 + \sqrt{R_t R_b}\,\exp(-2\alpha d)]^2 - 4\sqrt{R_t R_b}\,\exp(-2\alpha d)\cos^2(\Phi_{rt}/2)}\,. \tag{13}$$

Since the boundary conditions for the forward- and the backward-traveling amplitudes at the bottom mirror are the same for both cases, the standing-wave patterns are also the same, and Eq. (12) holds with a ξ that does not depend on the position z. It then directly follows that the effective saturation fluence of the A-FPSA compared with the saturation fluence of the material (i.e., the AR-coated sample) is divided by the same factor, or

$$E_{\mathrm{sat}}{}^{\mathrm{eff}} = \frac{1}{\xi} E_{\mathrm{sat}}{}^{0}. \tag{14}$$

At antiresonance ξ is smaller than unity. For our A-FPSA's we calculated for ξ a value typically between 0.007 and 0.018, depending on the top reflector as shown below. Equations (13) and (14) already show one of the main advantages of the A-FPSA: it is possible to vary the saturation fluence of the absorber by varying any of the device parameters R_t, d, or α (the absorption edge). We can vary R_t by adjusting the number of dielectric layer pairs of the top mirror. In Fig. 2 the calculated insertion losses $l = 1 - R$ for low intensities, Fig. 2(a), and the ξ factor, Fig. 2(b), are depicted as a function of the reflectivity of the top mirror for varying absorber thicknesses d. The other parameters have been chosen as shown in Fig. 1, with $\alpha = 0.34\ \mu\mathrm{m}^{-1}$ and $n = 3.2$. The result for $d = 0.61\ \mu$m corresponds to the actual samples that we have used for the mode-locking experiments. One can see that decreasing R_t means increasing the insertion losses as well as decreasing the saturation fluence. On the other hand, one can achieve the same effect by increasing the thickness d, but then the increase in ξ is reduced.

For a passively mode-locked solid-state laser the most important parameters besides the recovery time are the cw saturation intensity and the saturation fluence in pulsed mode. We consider the two cases of a cw signal and of a pulse whose duration is much shorter than the absorber recovery time or the carrier lifetime τ_c. In the first case the saturation is determined by the cw saturation intensity I_{sat} and in the second case by the saturation fluence E_{sat} (Ref. 22):

$$I_{\mathrm{sat}} = \frac{h\nu}{\sigma\tau_c}, \qquad E_{\mathrm{sat}} = \frac{h\nu}{\sigma}, \qquad I_{\mathrm{sat}} = \frac{E_{\mathrm{sat}}}{\tau_c}, \tag{15}$$

where σ denotes the absorber cross section, I_{sat} the saturation intensity, and E_{sat} the saturation fluence. In the mode-locked state the time interval T_R between consecutive pulses is given by the cavity round-trip time, which is of the order of 10 ns. We then obtain for the cw and pulsed saturation, assuming a carrier lifetime of 10 ps,

$$\frac{E}{E_{\mathrm{sat}}} = \frac{T_R I}{\tau_c I_{\mathrm{sat}}} \approx 1000\,\frac{I}{I_{\mathrm{sat}}}, \tag{16}$$

which means that the absorber is more strongly bleached in the pulsed mode.

For the case of an AR-coated sample the change in reflectivity induced by a pulse whose duration is short compared with the absorption recovery time can be calculated from the common traveling-wave rate equations.[22,23] If R_0 is the unsaturated low-intensity reflectivity of the sample, the final reflectivity R_f after the pass of a pulse of energy E_{in} is given by

$$R_f = \frac{R_0}{R_0 - (R_0 - 1)\exp(-E_{\mathrm{in}}/E_{\mathrm{sat}})}, \tag{17}$$

and the reflectivity that the pulse itself experiences is

$$R(E_{\mathrm{in}}) = \frac{E_{\mathrm{out}}}{E_{\mathrm{in}}} = R_{\mathrm{ns}}\,\frac{\log\left(\dfrac{R_0 - 1}{R_f - 1}\right)}{\log\left(\dfrac{R_0 - 1}{R_f - 1}\right) - \log\left(\dfrac{R_0}{R_f}\right)}, \tag{18}$$

where we have introduced R_{ns} to describe the nonsaturable part of the losses α_{ns}, i.e., $R_{\mathrm{ns}} = R(E_{\mathrm{in}} \to \infty) = \exp(-4\alpha_{\mathrm{ns}}d)$. Included in R_{ns} are the reflectivity of the bottom mirror R_b, scattering losses that are due to impurities at the surface of the sample, and losses introduced by free-carrier absorption. This is, in fact, not precisely correct, since one has to take into account that part of the nonsaturable losses is distributed along the absorber and enters the rate equations, which in this case can no longer be solved analytically. From a phenomenological point of view, however, we used Eqs. (17) and (18) to fit the experimentally measured $R(E_{\mathrm{in}})$ to obtain E_{sat} and R_{ns} and to calculate the corresponding reflectivity of the A-FPSA. As we show in Section 3, Eq. (18) gives an excellent fit to the measured data, thus justifying our simple model.

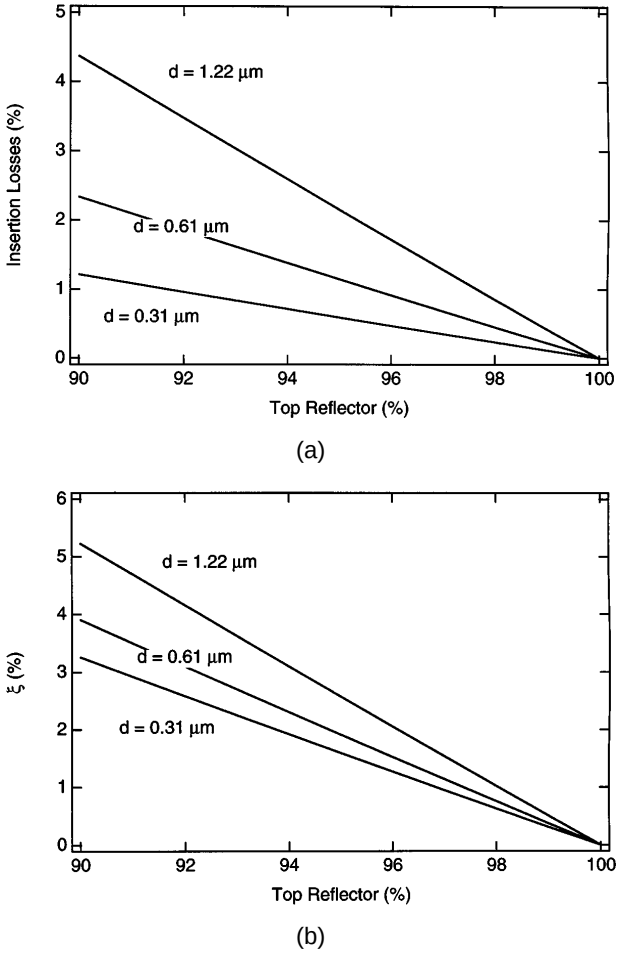

Fig. 2. (a) Calculated insertion losses, (b) ξ factor versus the reflectivity of the top mirror for various thicknesses d (0.31, 0.61, and 1.22 μm). Lines $d = 0.61\ \mu$m, the actual sample used in the mode-locking experiments.

One has to be aware that the saturation fluence measured in reflection is smaller than that measured in transmission because of standing-wave effects. The saturation fluence measured in reflection, however, is relevant for our case. To calculate the corresponding reflectivity change of the A-FPSA, we replace the term $\sqrt{R_b}\exp(-2\alpha d)$ in Eq. (11) with the effective saturated value $\sqrt{R(\xi E_{\mathrm{in}})}$, obtained from Eq. (18), and we obtain at antiresonance

$$R_{\mathrm{A-FPSA}}(E_{\mathrm{in}}) = \frac{[\sqrt{R_t} + \sqrt{R(\xi E_{\mathrm{in}})}]^2}{[1 + \sqrt{R_t R(\xi E_{\mathrm{in}})}]^2}. \tag{19}$$

E_{in} is now the incident pulse energy (or fluence) on the A-FPSA, and the factor ξ, Eq. (13), accounts for the reduction of intensity inside the absorber.

C. Mode-Locking Driving Force

To discuss the mode-locking buildup regime we have to consider the saturation of the A-FPSA for cw intensities. In this case Eqs. (17) and (18) can no longer be used to describe the reflectivity change, since the instantaneous absorption is now a function of the instantaneous intensity rather than of the integrated pulse energy, as it would be if the pulse duration were much shorter than the absorber recovery time. We write for the intensity $I(z)$ inside the absorber

$$\frac{\mathrm{d}I}{\mathrm{d}z} = -\frac{2\alpha_0}{1 + I/I_{\mathrm{sat}}} I. \tag{20}$$

Equation (20) is separable, and we obtain after integration over the length $2d$ for the reflectivity $R(I_{\mathrm{in}}) = I_{\mathrm{out}}/I_{\mathrm{in}}$ the transcendent equation

$$\log R + \frac{I_{\mathrm{in}}}{I_{\mathrm{sat}}}(R - 1) = -4\alpha_0 d, \tag{21}$$

which has to be solved numerically. Again, we incorporate standing-wave effects in I_{sat} in the same way as we have done for E_{sat}. Since $I_{\mathrm{in}}/I_{\mathrm{sat}} \ll E_{\mathrm{in}}/E_{\mathrm{sat}}$, we can restrict ourselves to the case $I_{\mathrm{in}}/I_{\mathrm{sat}} \to 0$. Equation (21) can then be written as

$$\log R + \frac{I_{\mathrm{in}}}{I_{\mathrm{sat}}}[\exp(-4\alpha_0 d) - 1] = -4\alpha_0 d \tag{22}$$

or

$$R(I_{\mathrm{in}}) = R_{\mathrm{ns}} \exp\left\{-\frac{I_{\mathrm{in}}}{I_{\mathrm{sat}}}[\exp(-4\alpha_0 d) - 1] - 4\alpha_0 d\right\}, \tag{23}$$

where the nonsaturable losses α_{ns} again have been taken into account by $R_{\mathrm{ns}} = \exp(-4\alpha_{\mathrm{ns}} d)$. In analogy to the pulsed case, the saturated cw reflectivity of an A-FPSA can now be calculated with $\sqrt{R_b}\exp(-2\alpha d)$ in Eq. (11) replaced by $\sqrt{R(\xi I_{\mathrm{in}})}$, obtained from Eq. (23). The saturation intensity can be calculated from Eqs. (15) with the measured values for E_{sat} and τ_c. This is also justified in the presence of standing-wave effects, since the spatial extension of the pulses is much larger than the dimension of the absorber.

An important parameter for a mode-locked or self-Q-switched solid-state laser is the mode-locking driving force of the absorber, which we defined as $\mathrm{d}R/\mathrm{d}I$ for $I \to 0$. This parameter is directly related to the self-amplitude-modulation coefficient γ as used in standard mode-locking theories.[24] We carry out the derivative of Eq. (11) with respect to I by using Eq. (23) and obtain at antiresonance

$$\left(\frac{\mathrm{d}R}{\mathrm{d}I}\right)_{I=0} = \frac{\tau_c(R_t - 1)^2}{E_{\mathrm{sat}}} \frac{[\exp(4\alpha_0 d) - 1]\{\sqrt{R_t} + \sqrt{R_b}\exp[-2(\alpha_0 + \alpha_{\mathrm{ns}})d]\}\sqrt{R_b}\exp[-2(\alpha_0 + \alpha_{\mathrm{ns}})d]}{[\exp(2\alpha_0 d) + \sqrt{R_t R_b}]^2\{1 + \sqrt{R_t R_b}\exp[-2(\alpha_0 + \alpha_{\mathrm{ns}})d]\}^3}. \tag{24}$$

We can obtain a simpler approximate formula by setting $\sqrt{R_t} \approx \sqrt{R_b} \approx 1$ in the second factor on the right-hand side of Eq. (24):

$$\left(\frac{\mathrm{d}R}{\mathrm{d}I}\right)_{I=0} = \frac{\tau_c(R_t - 1)^2}{E_{\mathrm{sat}}} \times \frac{[1 - \exp(2\alpha_0 d)]\exp(-2\alpha_{\mathrm{ns}} d)}{[1 + \exp(2\alpha_0 d)]\{1 + \exp[-2(\alpha_0 + \alpha_{\mathrm{ns}})d]\}^2}. \tag{25}$$

The difference between Eq. (24) and the simpler formula (25) has been calculated to be only a few percent if both R_b and R_t are larger than 90%. These equations show the important result that the driving force of the A-FPSA is proportional to $\tau_c(R_t - 1)^2$ and inversely proportional to E_{sat}. In Fig. 3 the calculated driving force is shown as a function of the reflectivity of the top mirror R_t and of the absorber thickness d. The curve for $d = 0.61$ μm represents a sample with a 22-ps carrier lifetime and a saturation fluence of 48 $\mu\mathrm{J/cm^2}$, which has been used for the mode-locking experiments.

D. Group-Delay Dispersion of an A-FPSA

The equations derived above give an exact description of the A-FPSA only within the stop bands of the Bragg mirrors. For an exact calculation of the reflectivity, the phase Φ, the group delay $\mathrm{d}\Phi/\mathrm{d}\omega$, and the group-delay dispersion $\mathrm{d}^2\Phi/\mathrm{d}\omega^2$ within a broader wavelength range one has to use numerical methods. We calculated the complex reflectivity of our A-FPSA structures by using a standard transmission matrix model.[25] The calculated reflectivity and group delay of the structure depicted

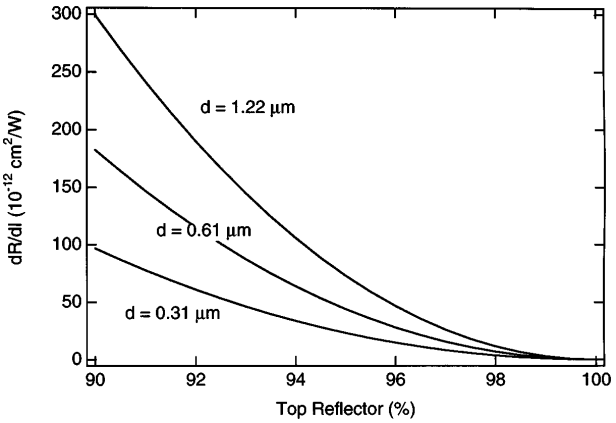

Fig. 3. Calculated mode-locking driving force versus reflectivity of the top mirror for various thicknesses d (0.31, 0.61, and 1.32 μm). Curve $d = 0.61$ is the actual sample, with a 22-ps carrier lifetime and a saturation fluence of 48 $\mu\mathrm{J/cm^2}$, used in the mode-locking experiments.

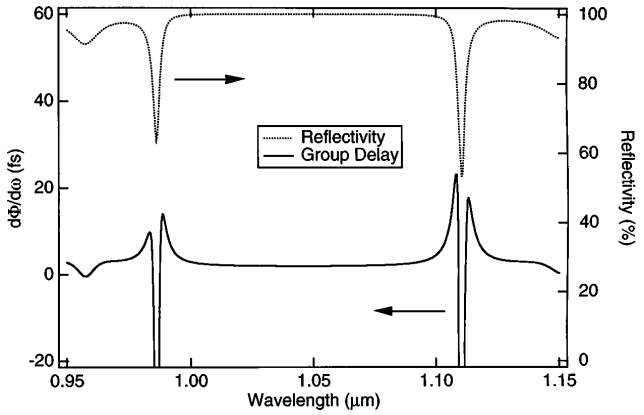

Fig. 4. Calculated reflectivity and group delay of an A-FPSA as shown in Fig. 1, with a top mirror consisting of four layer pairs ($R_t = 98\%$).

in Fig. 1 with a top mirror consisting of four pairs of TiO_2–SiO_2 layers (i.e., $R_t = 98\%$) are shown in Fig. 4. The group-delay dispersion of the A-FPSA is negligible within the free spectral range because the high-finesse Fabry–Perot cavity is operated at antiresonance. This is in contrast to a low-finesse Fabry–Perot cavity, e.g., a Gires–Tournois cavity, for which considerable group-delay dispersion is achieved over the whole wavelength range; this effect, under certain circumstances, can be used for pulse compression.[26] It can be seen from Fig. 4 that within a range of ≈100 nm the group delay is almost constant, i.e., 2 fs ± 0.5 fs, and the group-delay dispersion therefore is almost zero. It should thus be possible, in principle, to sustain pulses with durations approaching 10 fs. A nearly constant saturable absorption over the free spectral range can be achieved when the band gap of the absorbing layer is varied through variation of the indium content during growth.[27]

E. Nonlinear Phase Effects

Besides amplitude effects that are due to absorption bleaching, the A-FPSA also introduces phase effects that are due to refractive-index changes dominated by the photogenerated carrier density. A change of refractive index in the absorber layer, in principle, shifts the position of the resonances, but this shift does not produce any nonlinear reflectivity changes as long as we are operating at antiresonance within the free spectral range. However, one has to take into account that an intensity-dependent refractive index in the absorber can act as a focusing lens. To give an estimation of the upper limit of this effect, we assume an increase in refractive index of $\Delta n = 0.01$ for a generated carrier density of $N = 10^{18}$ cm^{-3} (Ref. 28) at the position of the peak intensity of the pulse. From numerical calculations[25] we obtain a change in phase of the reflectivity at 1050 nm for only $\Delta\Phi = 0.0005$ for a top mirror consisting of four layer pairs ($R_t = 98\%$) and $\Delta\Phi = 0.0012$ for three layer pairs ($R_t = 95\%$). Since this phase shift depends on the incident optical intensity with a Gaussian distribution, its effect can be described by an effective lens with a focal length of several meters, which, like KLM, can lead to an effective saturable absorber. However, in comparison with the nonlinear reflectivity change, this free-carrier-induced nonlinear lens gives a negligible contribution to the mode locking, as *ABCD* calculations have shown.[22] Furthermore, we can also neglect the effect of a nonlinear frequency chirp arising from self-phase modulation in the absorber compared with the nonlinear phase change that is due to the laser crystal. For example, the phase change after one pass through a crystal of 4-mm length with an n_2 of 2.8×10^{-16} cm^2/W (Nd:glass) of the peak of a 10-ps pulse with a peak power of 20 kW is $\Delta\phi_{\text{peak}} = 0.0004$, assuming a spot size in the crystal of 3×10^{-4} cm^2.[12] The peak phase change of a 100-fs pulse with 2-MW peak power is $\Delta\phi_{\text{peak}} = 0.04$. The phase change induced by the absorber is thus comparable with the phase change of a picosecond pulse caused by the laser crystal but more than 1 order of magnitude smaller than the phase change of a femtosecond pulse caused by the laser crystal. The phase modulation through the absorber is a slow effect; it therefore does not depend on the pulse duration once the pulses are shorter than the carrier lifetime. Again, it is the HR top mirror that reduces the effects of the absorber on the pulse. The effect of a nonlinear phase shift might become important in the case of a low-reflectivity top mirror and can contribute positively or negatively to the total effective gain, depending on the cavity design.

F. Design Criteria for an A-FPSA

We are now able to draw several conclusions for the design of an A-FPSA. The parameters that can be varied to adapt the absorber to the requirements of a solid-state laser are the material parameters α_0, E_{sat}, and τ_c as well as the device parameters R_t (i.e., the number of dielectric layer pairs) and d. As we show in Section 3, the material parameters can be adjusted within a certain range by variation of the growth temperature (E_{sat} and τ_c) and the indium content or the quantum-well thickness (α_0). The reflectivity of the bottom reflector should in any case be as close to 100% as possible, since any reduction contributes to the nonsaturable losses. That is, however, typically not critical, since the influence of R_b on the insertion losses is strongly reduced in an A-FPSA with a HR top mirror. Increasing the thickness d has the same effect as increasing α_0: an increase in losses and a weak increase in ξ (thus a weak decrease of the effective saturation fluence E_{sat}/ξ and an increase of the driving force $\mathrm{d}R/\mathrm{d}I$). The same can be achieved by a decrease in the top reflectivity R_t (see Figs. 2 and 3). So far there is the trade-off that increasing the driving force leads to an increase in intracavity losses. With our LT-grown semiconductor absorbers, however, we have the additional possibility of increasing the driving force by increasing the carrier lifetime or simply by reducing the spot size on the A-FPSA without affecting the losses.

3. EXPERIMENTAL DETERMINATION OF THE PARAMETERS

For the measurements we used five samples that were grown by molecular-beam expitaxy at different substrate temperatures (200, 260, 315, 340, and 380 °C) but are otherwise identical, with the top mirror replaced by an AR coating. Samples from the same epitaxial runs with top mirrors with reflectivities of 95% or 98% have been used as A-FPSA's in various mode-locking experiments with Nd:YAG, Nd:YLF, and Nd:glass lasers.[11,15] The

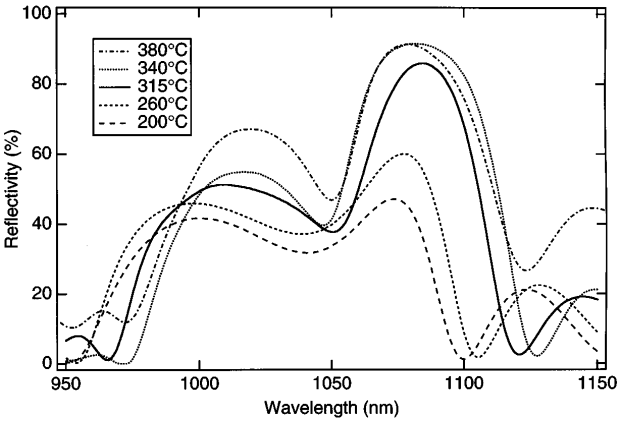

(a)

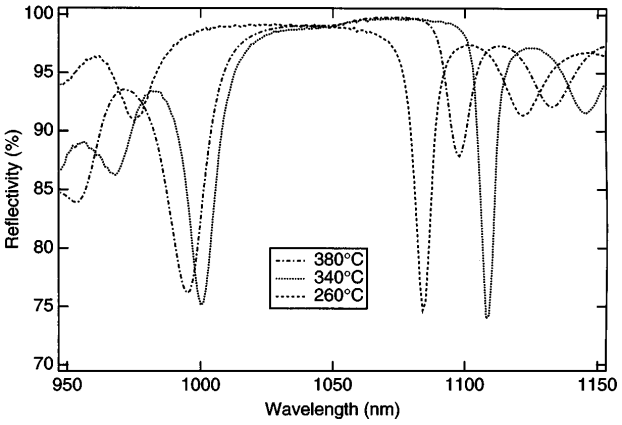

(b)

Fig. 5. Low-intensity reflectivity of (a) AR-coated samples and (b) A-FPSA's grown at various temperatures.

low-intensity reflectivity (shown in Fig. 5) has been measured absolutely with a Varian Cary 5E spectrophotometer. All curves show a dip near 1050 nm resulting from the exciton resonance, which broadens for lower growth temperatures. The minima above 1100 nm and below 1000 nm are caused by the bandwidth of the bottom mirror. The reflectivity of three corresponding A-FPSA's (i.e., with a HR top mirror) is shown in Fig. 5(b). As expected, the reflectivity is close to unity at antiresonance, but a slight variation that is due to the varying absorption can still be seen. The sharp minima near 1000 and 1100 nm are resonances. The useful spectral range in all three samples is >100 nm.

The absorber recovery time has been determined with a standard degenerate noncollinear pump–probe experiment, with perpendicular polarizations to eliminate coherent artifacts, by use of 120-fs pulses from a Ti:sapphire laser. The probe beam was strongly attenuated compared with the pump beam. We also used a low-duty-cycle (1:20) acousto-optic modulator to gate the pump and the probe beams to eliminate heating effects. Figure 6(a) shows a typical bitemporal impulse response of the sample grown at 260 °C for different pump-pulse energies and a wavelength of $\lambda = 1060$ nm. The first, fast decay constant of the order of 200 fs is due to intraband thermalization, and the subsequent slower time constant is associated with carrier recombination. Since the slow time constant determines the cw saturation intensity, it is important in the picosecond, mode-locking buildup regime. The carrier lifetimes of different samples are summarized in Fig. 6(b). The dependence on the growth temperature is evident. It is thus possible to choose a lifetime within several picoseconds as long as several tens of picoseconds simply by adjustment of the growth temperature. The upper limit for the growth temperature is set by the onset of crosshatched surface roughness, leading to high nonsaturable scattering losses.

The saturation fluence E_{sat} and the nonsaturable background losses $\Delta R_{ns} \equiv 1 - R_{ns}$ have been determined from the measured average reflectivity as a function of incident pulse energy density on the AR-coated samples [Fig. 7(a)]. For this measurement we increased the pulse duration to ≈1.4 ps to determine the saturation fluence of the thermalized carrier distribution, which is relevant for the picosecond mode-locking buildup regime. The measured data have been fitted to a function of the form of Eq. (18) to yield E_{sat} and ΔR_{ns}. As is shown in Fig. 7(a), Eq. (18) gives an excellent fit of the data, thus confirming our model. The results for different samples are summarized in Fig. 7(b). The saturation fluences and the nonsaturable losses for $\lambda = 1040$ nm and $\lambda = 1060$ nm are depicted as a function of growth temperature. As

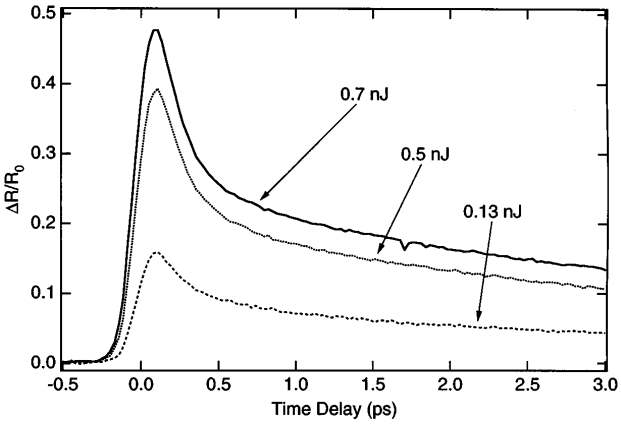

(a)

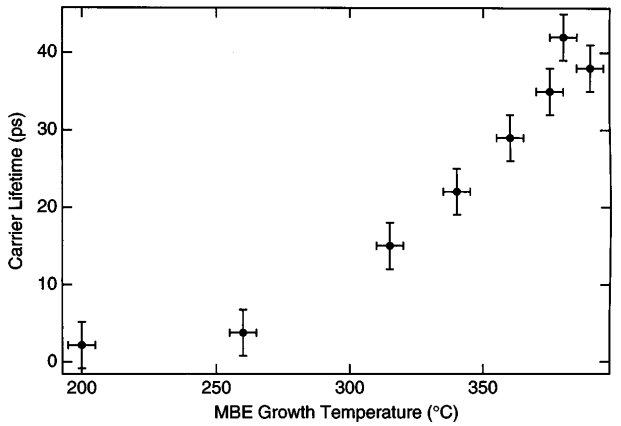

(b)

Fig. 6. (a) Typical bitemporal pulse response of the sample grown at 260 °C for various pulse energies (0.13, 0.5, and 0.7 nJ; $\lambda = 1060$ nm); (b) measured carrier lifetimes versus growth temperature. MBE, molecular-beam epitaxy.

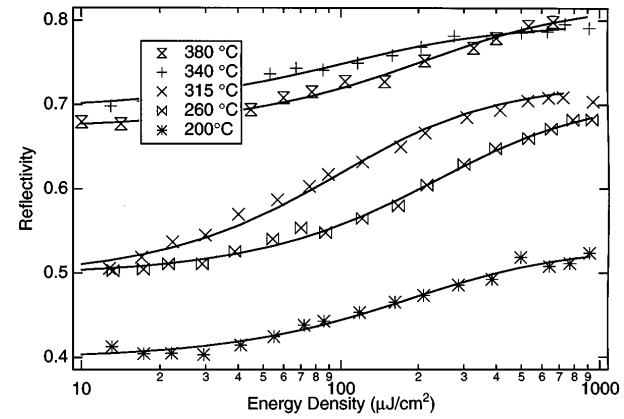

(a)

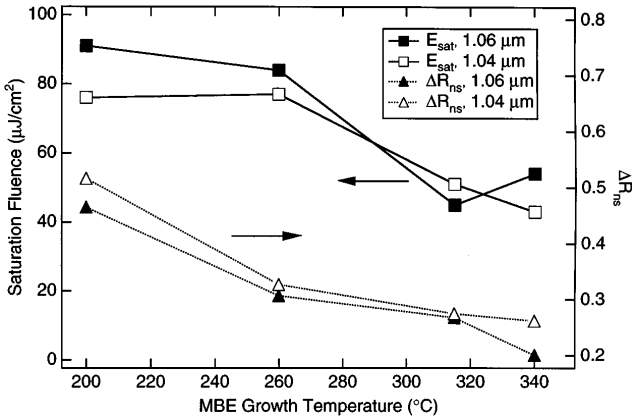

(b)

Fig. 7. (a) Measured change in reflectivity versus pulse energy density (symbols) and theoretical fit (solid curves); (b) saturation fluence and nonsaturable losses for samples grown at various temperatures.

expected, the nonsaturable losses increase for decreasing growth temperature, but their influence is strongly reduced for an A-FPSA with a HR top mirror. However, the nonsaturable losses reduce the total amount of nonlinear reflectivity change that can be achieved. E_{sat} also shows an increase for decreased growth temperature that is due to a reduction of the absorption cross section.

The measurements at different wavelengths (1000, 1020, 1040, and 1060 nm) showed, as expected, a higher saturation fluence for shorter wavelengths (137, 97, 50, and 45 μJ/cm^2, respectively, for the sample with a growth temperature of 315 °C and similar results for samples), which results in smaller nonlinearities at shorter wavelengths. In general, however, the variations of the saturation fluence in the region of interest (between 1040 and 1060 nm) are of the order of only several percent [Fig. 7(b)].

Knowing α_0, α_{ns} (from ΔR_{ns}), E_{sat}, and τ_c, we are able to calculate the losses and the saturation behavior of an A-FPSA with the help of Eqs. (19) and (24) derived in Section 2. In Table 1 the calculated driving forces from Eq. (24) and the insertion losses are summarized for various samples that were used in the mode-locking experiments. The results show, as expected, how critically the driving force depends on the reflectivity of the top mirror and on the absorber recovery time. Also, the insertion losses increase from ≈0.4% for a 98% reflector to ≈1% for a 95% reflector, but they are much less dependent on the growth temperature.

At 1060 nm both the driving force and the insertion losses are reduced because of the smaller unsaturated absorption (see Fig. 5). However, the sample is heated as a result of the nonradiative recombination of the carriers, leading to a red shift of the absorption edge. By measuring the reflectivity of the samples with a varying duty cycle of the acousto-optic modulator, we found that for ≈4000-W/cm^2 intensity incident upon an AR-coated sample at 1060 nm the same reflectivity was reached as with 1047 nm. This corresponds to ≈200-kW/cm^2 intensity on an A-FPSA (95% reflector top mirror), a value that typically is reached in our laser cavities. In contrast, the reflectivity at 1047 nm did not change so much for an increasing duty cycle. It is thus reasonable also to use the values for 1047 nm when the samples are operated at 1060 nm. Because of the large free spectral range of the A-FPSA, heating does not affect the performance at antiresonance. Thus no cooling or any other thermal control is required.

The calculated change in reflectivity as a function of the incident pulse energy density for the same samples at 1047 nm is depicted in Fig. 8. Since the absorber is almost unsaturated in cw operation, the curves show the total change in reflectivity when the laser changes from cw to pulsed operation. This total change is of the order of ≈0.2% for a 98% top reflector and 0.5% for a 95% top reflector, provided that the absorber can be bleached completely. This is, however, not the case in general, as we show in Section 4. Note that the slope of the reflectivity in Fig. 8 for the low energy densities has nothing to do with the above-defined mode-locking driving force for cw intensity, since the saturation behavior in the pulsed mode differs from the cw saturation as explained in Section 2. The slope of the curves in Fig. 8 depends only on the saturation fluence E_{sat} and not on the absorber recovery time.

Table 1. Mode-Locking Driving Forces and Insertion Losses of Various A-FPSA's with 95%- and 98%-Reflectivity Top Mirrors Used in the Mode-Locking Experiments

		dR/dI (10^{-12} cm^2/W)		Insertion Loss (%)	
Sample	τ_c (ps)	95%	98%	95%	98%
260 °C, 1047 nm	3.8	3.51	0.55	1.11	0.44
315 °C, 1047 nm	15	22.7	3.54	1.00	0.40
340 °C, 1047 nm	22	44.0	6.89	1.14	0.45
380 °C, 1047 nm	40	45.9	7.18	0.95	0.37
340 °C, 1060 nm	22	9.38	1.46	0.49	0.19
380 °C, 1060 nm	40	12.5	1.95	0.53	0.21

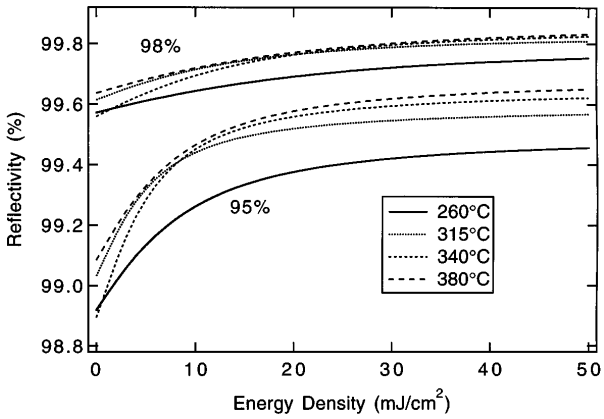

Fig. 8. Calculated reflectivity change versus pulse energy density of different A-FPSA's with 95% and 98% reflectivity top mirrors at $\lambda = 1047$ nm.

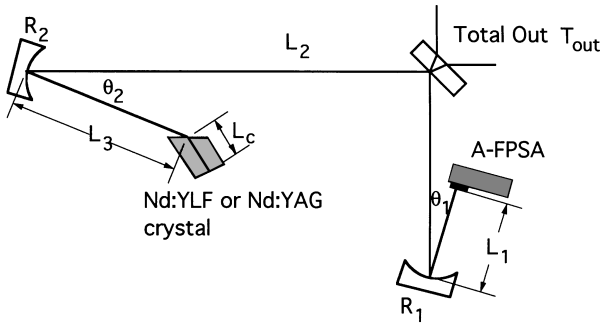

Fig. 9. Passively mode-locked gain-at-the-end Nd:YLF or Nd:YAG cavity with one of the end mirrors replaced by an A-FPSA.

4. EXAMPLES

A. Passively Mode-Locked Nd:YAG Laser

As a representative example we discuss in more detail a Nd:YAG laser pumped by a Ti:sapphire laser.[12] Similar results, however, were achieved with a Nd:YLF laser and with diode laser pumping.[11,13] In this section we present a detailed quantitative discussion for A-FPSA mode locking and compare it with KLM, which, as we show, is typically negligible in the picosecond regime.

We used the following parameters of the gain-at-the-end Nd:YAG cavity (Fig. 9): an A-FPSA with an $R_t \approx 95\%$ and a carrier lifetime of ≈40 ps (380 °C growth temperature). The cavity parameters are given by $\theta_1 = 8°$, $L_2 = 53$ cm, $\theta_2 = 10°$, $R_2 = 20$ cm, $L_3 = 9.9$ cm, and $L_c = 4$ mm. To vary the spot size on the A-FPSA, we chose in one case $R_1 = 10$ cm and $L_1 = 5.3$ cm, giving a spot area of 3.5×10^{-5} cm^2 and a pulse-repetition rate of 218 MHz, and in the other case $R_1 = 5$ cm and $L_1 = 2.56$ cm, giving a spot size of 8.1×10^{-6} cm^2 and a pulse-repetition rate of 227 MHz. In both cases L_1 is adjusted for the middle of the cavity stability regime, which we confirmed experimentally by moving the A-FPSA sample in both directions until it stopped lasing.

The Nd:YAG crystal is cut on one side at Brewster's angle and on the other side flat, with an AR coating for the pump wavelength of 808 nm and an HR coating for the lasing wavelength of 1.06 μm. The Nd:YAG laser is pumped with a cw Ti:sapphire laser at a wavelength of 808 nm and a measured pump radius of 20 μm.

The mode locking is always self-starting, and the threshold for pulse formation depends on the incident energy density on the A-FPSA. With the smaller spot size of 8.1×10^{-6} cm^2 on the A-FPSA ($R_1 = 5$ cm), the mode locking starts at ≈6-W average intracavity power or at ≈3.3-mJ/cm^2 pulse energy density. Increasing the spot size to 3.5×10^{-5} cm^2 ($R_1 = 10$ cm) increases the pulse-formation threshold to ≈14-W average intracavity power with ≈2-mJ/cm^2 pulse energy density. The slightly lower pulse energy density for the onset of mode locking can be explained with the higher small-signal gain at the higher pump power, which produces a shorter mode-locking buildup time.[11]

It has been observed that the pulse width decreases with higher intracavity power because of the larger nonlinear reflectivity change in the A-FPSA[12] (Fig. 10). The final pulse duration is limited by the gain bandwidth of the Nd:YAG laser and the total intracavity losses. The steady-state pulse duration is 10.5 ± 0.2 ps with a 1.5% output coupler and 12.3 ± 0.2 ps with a 2.8% output coupler, which is shorter than the carrier lifetime of 40 ps, thus showing that the fast component of the absorber can support shorter pulses.

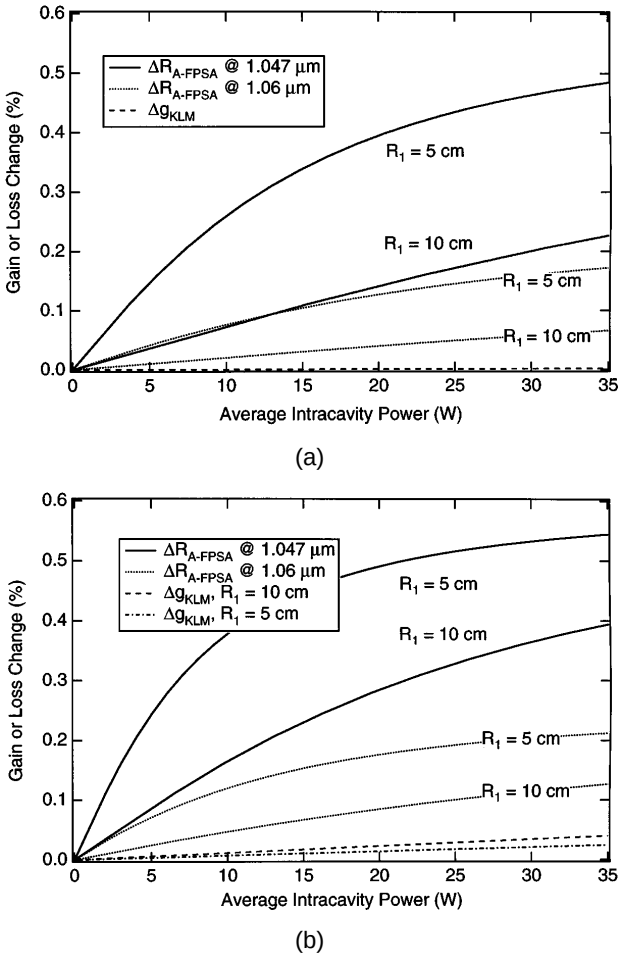

Fig. 10. Comparison of gain or loss change of KLM and A-FPSA's versus the average intracavity power in a mode-locked Nd:YAG laser (a) in the middle of the stability regime and (b) close to the stability limit.

To estimate the contribution of KLM, we can calculate the gain increase Δg that is due to gain aperturing from an *ABCD*-matrix model, because there is no hard aperture present inside the laser.[7,12,22] The calculations are simple because the model radius, the mode change that is due to self-focusing, and the pump-beam radius are approximately constant along the Nd:YAG crystal. We furthermore neglect the hard aperture caused by the resonator itself, since the mode size on the laser mirrors [inch or half-inch mirrors (1 in. = 2.54 cm)] never exceeds 600 μm, and diffraction losses are negligible.

In comparison, Eq. (19) determines the loss reduction of the A-FPSA between pulsed and cw oscillations. The results are shown in Fig. 10 together with the calculated gain change for 10-ps pulses resulting from KLM for a cavity in the middle of the stability regime [Fig. 10(a)] and close to the stability limit [Fig. 10(b)].

In the middle of the cavity stability regime KLM is much weaker than the nonlinear loss reduction from the A-FPSA. At an average intracavity power of 35 W we determined a nonlinear gain increase Δg of only 0.0006%. At the stability limit with a longer L_1 we calculate a mode increase that is due to self-focusing, which actually produces a gain reduction and therefore does not support mode-locked operation. For a shorter L_1 close to the stability limit we obtain a larger KLM contribution, which is, however, still much weaker than the A-FPSA contribution [Fig. 10(b)].

The mode-locking driving force for KLM, $\mathrm{d}(\Delta g)/\mathrm{d}I$, in the middle of the cavity stability regime is calculated to be $\approx 8 \times 10^{-10}$ W^{-1} and for a shorter L_1 close to the stability limit $\approx 3 \times 10^{-10}$ W^{-1}.[12] In comparison the mode-locking driving force for the A-FPSA is $\approx 10^{-5}$ W^{-1} for $R_1 = 5$ cm and $\approx 10^{-6}$ W^{-1} for $R_1 = 10$ cm, typically a factor of 1000 larger. This explains why the A-FPSA efficiently starts passive mode locking. The contribution of KLM in diode-pumped solid-state lasers is typically reduced even further, because the mode area in the gain area is larger. With an A-FPSA, self-starting diode-pumped mode-locked Nd:YAG lasers have been demonstrated.[13]

B. Self-Q Switching

From the theory of passive mode locking[29] it is expected that the laser starts will become unstable against self-Q switching if the driving force or the intracavity losses become too high. In Ref. 29 the condition for self-Q switching is derived [inequality (28) of Ref. 29], which can be written in the following form:

$$\left|\frac{\mathrm{d}R}{\mathrm{d}I}\right| I > \frac{g_0}{g_{\mathrm{sat}}}\,\frac{T_R}{\tau_2}\,, \tag{26}$$

with the unsaturated gain g_0 (determined by the pump power), the saturated gain g_{sat} (i.e., the intracavity losses), the round-trip time T_R, and the laser's upper-state lifetime τ_2. Inequality (26) permits a qualitative discussion: the tendency for self-Q switching is increased for a high driving force, high losses, a high repetition rate (i.e., low pulse energy), and a longer upper-state lifetime. On the other hand, increasing the pump power reduces the tendency for self-Q switching and leads to stable mode locking. These tendencies were verified in experiments with mode-locked Nd:YLF lasers that include A-FPSA's.[11]

In Fig. 11 the relaxation oscillation peak of the microwave spectrum, indicating the Q-switched envelopes of the pulse train, is depicted as a function of pump power for A-FPSA's grown at different temperatures. The sudden decrease of the relaxation oscillation peak at a certain pump power indicates the transition to stable mode locking. The cavity design of the Nd:YLF laser was the same as that depicted in Fig. 9. As expected, a higher pump power is required for stable mode locking if samples with longer recovery times (i.e., higher driving forces) are used. We can now insert numerical values into inequality (26), e.g., for the sample with a 15-ps lifetime (315 °C) and a 3.5×10^{-5}-cm^2 spot size at 1 W pump power, and get for the left-hand side of the inequality 1.1×10^{-5} (with 4.8×10^5 W/cm^2 intensity on the absorber) and for the right-hand side 10^{-3} (with $g_0/g_{\mathrm{sat}} = 100$, $T_R = 4.5$ ns, and $\tau_2 = 450$ μs). This would imply that the condition for Q switching could never be fulfilled, and mode locking would always be stable. Inequality (26), however, holds only for pure Q switching without any mode-locked substructure. In fact, pure Q switching has never been observed in the experiments but has always been accompanied by a mode-locked substructure. One can therefore not expect inequality (26) to give a quantitative exact criterion for the stability of the pulses, but the tendencies are described correctly and verified by the experiments.

C. Mode-Locking Buildup Time

In Ref. 11, the starting dynamics of the Nd:YLF laser (Fig. 9) was investigated experimentally. In Fig. 12 the mode-locking buildup time is shown for various samples as a function of the pump power. In Eqs. (18)–(20) of Ref. 29, the condition for self-starting of passive mode locking with a saturable absorber was derived. If we assume that we are well above the threshold for self-starting, then the growth rate of a perturbation of the amplitude per round-trip time is given by the left-hand side of inequality (20) of Ref. 29. In our case, for which the absorber recovery time is much shorter than the cavity round-trip time T_R, we calculate the growth rate to be

$$T_{\mathrm{growth}} = T_R\left(\frac{\mathrm{d}R}{\mathrm{d}I}\,I\right)^{-1}, \tag{27}$$

and we obtain for the same case as in Subsection 4.B, i.e., for the 15-ps sample at 1 W of pump power, $T_{\mathrm{growth}} =$

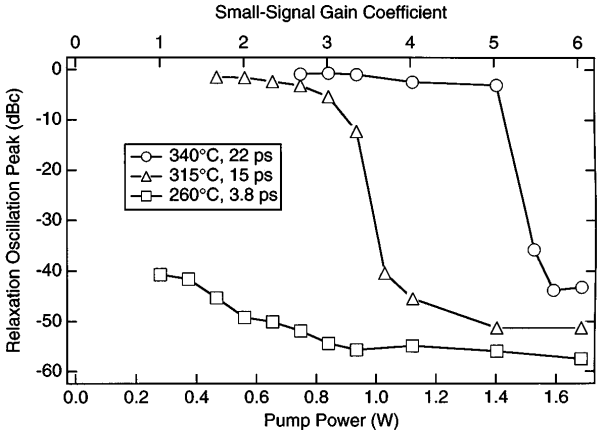

Fig. 11. Measured relaxation oscillation peak of the microwave spectrum of a mode-locked Nd:YLF laser with various A-FPSA's.

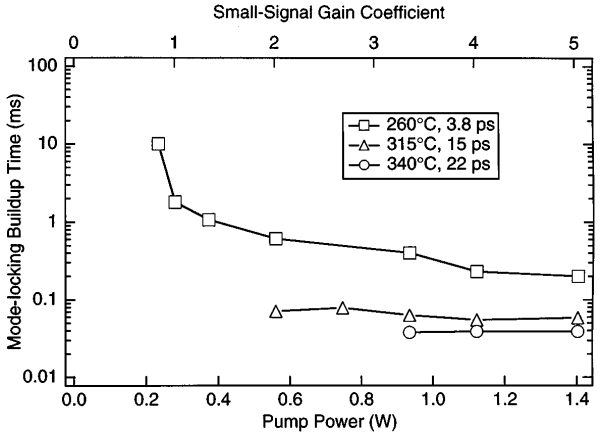

Fig. 12. Measured mode-locking buildup time of a mode-locked Nd:YLF laser with various A-FPSA's.

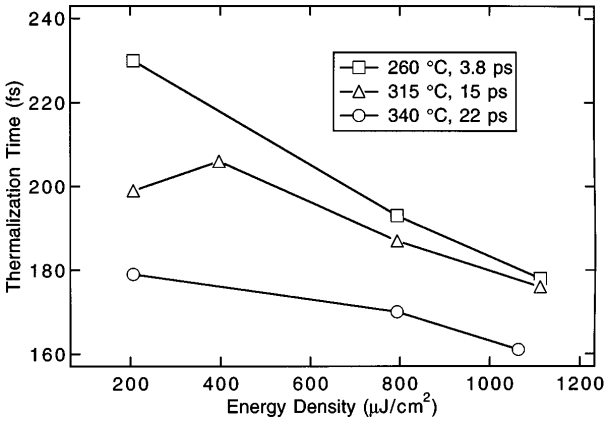

Fig. 13. Measured fast time constant (thermalization time) versus incident pulse energy for three different samples at 1060 nm.

400 μs. In the experiments (Fig. 12) a buildup time of $\approx$60 μs has been found. The simple formula (27) thus overestimates the buildup time by $\sim$1 order of magnitude, but the prediction that it is inversely proportional to the absorber recovery time (by means of the driving force) is verified in the experiment (see Fig. 12 and Table 1). We have measured buildup times of 200, 60, and 40 μs for the samples with τ_c equal to 3.8, 15, and 22 ps, respectively, at $\approx$1 W of pump power.

5. FEMTOSECOND REGIME

Recently the A-FPSA was used successfully to mode lock a Nd:glass laser, resulting in pulses with shorter than 100-fs duration.[15,16] As already mentioned, the temporal response of an A-FPSA shows a fast time constant of the order of 200 fs that is due to intraband thermalization of the photoexcited carriers [Fig. 6(a)]. A picosecond pulse therefore still sees a fast component of the saturable absorption, leading to further pulse shortening and stabilization. In Fig. 13 the measured fast time constant is shown as a function of the incident pulse energy density for three different samples. The excitation wavelength was 1060 nm, thus close to the band gap. As expected, the thermalization time decreases the increasing pulse energy, since the density of the photogenerated carriers becomes higher. In addition the thermalization time is reduced for samples grown at higher temperatures. This agrees with the experimental observation that shorter pulses can be produced when samples grown at higher temperatures are used (i.e., 140 fs for a 340 °C sample and 160 fs for a 315 °C sample[15]). In all the Nd:glass experiments the effect of KLM is comparable with the nonlinear reflectivity change of the A-FPSA in pulsed mode, but the cw mode-locking driving force of the A-FPSA is still several orders of magnitude higher than that due to Kerr lensing. This demonstrates the successful use of the fast thermalization time in a semiconductor to realize a fast saturable absorber for passive mode locking of a femtosecond rare-earth solid-state laser, as was also demonstrated previously with a color-center laser with an InGaAs–InAlAs MQW used as the fast saturable absorber.[30] The influence of the fast time constant on the pulse-formation process is under further investigation.

As shown in Section 2, pulse-broadening phase effects such as group-delay dispersion are negligible because the A-FPSA is operated at antiresonance. Within the $\approx$100 nm-wide free spectral range the variation of the group delay are less than $\pm$1 fs.

6. CONCLUSIONS

We have presented a detailed quantitative description of the saturation behavior of A-FPSA's as used in various passively mode-locked neodymium-doped solid-state lasers. Mode locking has always been self-starting because of the $\approx$1000-times-stronger mode-locking driving force compared with that for KLM. In the picosecond regime of standard Nd:YLF and Nd:YAG lasers the total nonlinear change in reflectivity in pulsed mode compared with that for cw operation is much larger than the change in gain that is due to Kerr lensing. This also holds when the laser is operated close to the limits of the stability regime.

The material and design parameters allow for a flexible adjustment of the relevant parameters, such as saturation intensity, saturation fluence, and insertion losses, which now can be adapted to the requirements of special solid-state lasers, determined among other things by upper-state lifetime and gain cross section. Choosing the proper mode-locking driving force and insertion losses is important to provide efficient self-starting of the mode-locked pulsation and to stabilize it against Q switching. On the other hand, one can obtain Q-switched pulses by increasing the recovery time or increasing the insertion losses of the A-FPSA[11] if it is so required by the application. With the A-FPSA, however, the Q-switched pulses have always been accompanied by a mode-locked substructure in our experiments.

The fact that the A-FPSA is always self-starting removes the constraint of operating the laser close to the limit of the stability regime. This gives much more freedom in the cavity design, which is important for the investigation of novel laser materials or structures such as compact and monolithic ultrafast solid-state lasers. Furthermore, the device offers distinct advantages for diode-pumped lasers when the mode size in the crystal has to be larger, thus reducing the effect of KLM.[13]

In addition, types III–V semiconductors cover a wide available wavelength range. With the (In)GaAs–

AlGaAs system the range between 0.7 and 1.6 μm can be attained and possibly extended to >2 μm by use of quaternary layers on InP. It may then be possible to use A-FPSA's to mode lock novel lasers with erbium-, holmium-, or thulium-doped crystals in a wavelength range that is of considerable interest for both optical communication and medical applications.

ACKNOWLEDGMENT

The authors acknowledge helpful discussions with F. X. Kärtner.

REFERENCES

1. K. J. Blow and D. Wood, "Mode-locked lasers with nonlinear external cavities," J. Opt. Soc. Am. B **5,** 629–632 (1988).
2. P. N. Kean, X. Zhu, D. W. Crust, R. S. Grant, N. Landford, and W. Sibbett, "Enhanced mode locking of color-center lasers," Opt. Lett. **14,** 39–41 (1989).
3. E. P. Ippen, H. A. Haus, and L. Y. Liu, "Additive pulse mode locking," J. Opt. Soc. Am. B **6,** 1736–1745 (1989).
4. D. E. Spence, P. N. Kean, and W. Sibbett, "60-fsec pulse generation from a self-mode-locked Ti:sapphire laser," Opt. Lett. **16,** 42–44 (1991).
5. U. Keller, G. W. 't Hooft, W. H. Knox, and J. E. Cunningham, "Femtosecond pulses from a continuously self-starting passively mode-locked Ti:sapphire laser," Opt. Lett. **16,** 1022–1024 (1991).
6. D. K. Negus, L. Spinelli, N. Goldblatt, and G. Feugnet, "Sub-100 femtosecond pulse generation by Kerr lens modelocking in Ti:sapphire," in *Advanced Solid-State Lasers*, G. Dubé and L. Chase, Vol. 10 of OSA Proceedings Series (Optical Society of America, Washington, D.C., 1991), pp. 120–124.
7. F. Salin, J. Squier, and M. Piché, "Mode locking of Ti:sapphire lasers and self-focusing: a Gaussian approximation," Opt. Lett. **16,** 1674–1676 (1991).
8. U. Keller, W. H. Knox, and H. Roskos, "Coupled-cavity resonant passive mode locked (RPM) Ti:sapphire laser," Opt. Lett. **15,** 1377–1379 (1990).
9. P. M. Mellish, P. M. W. French, J. R. Taylor, P. J. Delfyett, and L. T. Florez, "All-solid-state femtosecond diode-pumped Cr:LiSAF laser," Electron. Lett. **30,** 223–224 (1994).
10. U. Keller, D. A. B. Miller, G. D. Boyd, T. H. Chiu, J. F. Ferguson, and M. T. Asom, "Solid-state low-loss intracavity saturable absorber for Nd:YLF lasers: an antiresonant semiconductor Fabry–Perot saturable absorber," Opt. Lett. **17,** 505–507 (1992).
11. U. Keller, T. H. Chiu, and J. F. Ferguson, "Self-starting and self-*Q*-switching dynamics of a passively mode-locked Nd:YLF and Nd:YAG laser," Opt. Lett. **18,** 217–219 (1993).
12. U. Keller, "Ultrafast all-solid-state laser technology," Appl. Phys. B **58,** 347–363 (1994).
13. K. J. Weingarten, U. Keller, T. H. Chiu, and J. F. Ferguson, "Passively mode-locked diode-pumped solid-state lasers using an antiresonant Fabry–Perot saturable absorber," Opt. Lett. **18,** 640–642 (1993).
14. M. H. Ober, M. Hofer, U. Keller, and T. H. Chiu, "Self-starting, diode-pumped femtosecond Nd:fiber laser," Opt. Lett. **18,** 1532–1534 (1993).
15. U. Keller, T. H. Chiu, and J. F. Ferguson, "Self-starting femtosecond mode-locked Nd:glass laser using intracavity saturable absorbers," Opt. Lett. **18,** 1077–1079 (1993).
16. F. X. Kärtner, D. Kopf, and U. Keller, "Sub-100 fs homogeneously and inhomogeneously broadened Nd:glass lasers," in *Ultrafast Phenomena*, Vol. 7 of 1994 OSA Technical Digest Series (Optical Society of America, Washington, D.C., 1994), p. 3.
17. G. L. Witt, R. Calawa, U. Mishra, and E. Weber, eds., *Low Temperature (LT) GaAs and Related Materials*, Vol. 241 of Materials Research Society Symposium Proceedings (Materials Research Society, Pittsburgh, Pa., 1992).
18. T. H. Chiu, U. Keller, M. D. Williams, M. T. Asom, and J. F. Ferguson, "Low-temperature growth of InGaAs/GaAs saturable absorbers for passively mode-locked solid-state laser applications," J. Electron. Mater. (to be published).
19. Y. Suematsu, S. Arai, and K. Kishino, "Dynamic single-mode semiconductor lasers with a distributed reflector," IEEE J. Lightwave Technol. **LT-1,** 161–176 (1983).
20. L. R. Brovelli and U. Keller, "Simple analytical expressions for the reflectivity and the penetration depth of a Bragg mirror between arbitrary media," submitted to Opt. Commun.
21. H. A. Macleod, *Thin-Film Optical Filters* (Hilger, Bristol, UK, 1985).
22. A. E. Siegman, *Lasers* (University Science, Mill Valley, Calif., 1986).
23. G. P. Agrawal and N. A. Olsson, "Self-phase modulation and spectral broadening of optical pulses in semiconductor laser amplifiers," IEEE J. Quantum Electron. **25,** 2297–2306 (1989).
24. E. P. Ippen, "Principles of passive mode locking," Appl. Phys. B **58,** 159–170 (1994).
25. P. Yeh, *Optical Waves in Layered Media* (Wiley, New York, 1988).
26. M. Beck, I. A. Walmsley, and J. D. Kafka, "Group delay measurements of optical components near 800 nm," IEEE J. Quantum Electron. **27,** 2074–2081 (1991).
27. G. R. Jacobovitz-Veselka, U. Keller, and M. T. Asom, "Broadband fast semiconductor saturable absorber," Opt. Lett. **17,** 1791–1793 (1992).
28. J. Manning, R. Olshansky, and C. B. Su, "The carrier-induced index change in AlGaAs in 1.3 μm InGaAsP diode lasers," IEEE J. Quantum Electron. **QE-19,** 1525–1530 (1983).
29. H. A. Haus, "Parameter ranges for cw passive mode locking," IEEE J. Quantum Electron. **QE-12,** 169–176 (1976).
30. M. N. Islam, E. R. Sunderman, C. E. Soccolich, I. Bar-Joseph, N. Sauer, T. Y. Chang, and B. I. Miller, "Color center lasers passively mode locked by quantum wells," IEEE J. Quantum Electron. **25,** 2454–2463 (1989).